Acta Crystallographica Section B
Structural Science
ISSN 0108-7681

Isostructural phase transition in *m*-carboxyphenylammonium monohydrogenphosphite

El-Eulmi Bendeif,[a] Slimane Dahaoui,[a] Michel François,[b] Nourredine Benali-Cherif[c] and Claude Lecomte[a]*

[a]Laboratoire de Cristallographie et Modélisation des Matériaux Minéraux et Biologiques LCM^{3}B CNRS UMR 7036, Université Henri Poincaré, Nancy 1, Faculté des Sciences, BP 239, 54506 Vandoeuvre-lès-Nancy CEDEX, France, [b]Laboratoire de Chimie du Solide Minéral CNRS UMR 7555, Université Henri Poincaré, Nancy 1, Faculté des Sciences, BP 239, 54506 Vandoeuvre-lès-Nancy CEDEX, France, and [c]Institut des Sciences Exactes, Technologie et Informatique Centre Universitaire de Khenchela 40000, Khenchela, Algeria

Correspondence e-mail: claude.lecomte@lcm3b.uhp-nancy.fr

Received 9 February 2005
Accepted 20 August 2005

Crystals of *m*-carboxyphenylammonium monohydrogenphosphite, $C_7H_8NO_2^+\cdot H_2PO_3^-$ (*m*-CPAMP), space group $P2_1/c$, grown from aqueous solution undergo a reversible first-order single-crystal phase transition at T_c = 246 (2) K with a hysteresis of 3.6 K. The thermal behaviour of the sample was characterized by differential scanning calorimetry (DSC) experiments. Variations of the unit-cell parameters *versus* temperature between 100 and 320 K are reported. The transition from the higher-temperature phase (HTP) to the lower-temperature phase (LTP) is characterized by a unit-cell volume contraction of 1.77%. The average structure and unit-cell packing of *m*-CPAMP at lower temperature (100 K) are reported from accurate X-ray data sets and compared with those of the higher-temperature phase (293 K) in order to investigate the mechanism of the phase transition. The reciprocal lattice reconstruction showed a few very weak satellite reflections which will be discussed in a forthcoming paper.

1. Introduction

Compounds consisting of amino acids with different inorganic acids or salts exhibit various types of structural phase transitions, some of those being ferroelectric substances. The best example known is triglycine sulfate (TGS; Matthias *et al.*, 1956), which is used as an IR detector; other members of this family are triglycine selenate (TGSe) and triglycine tetrafluoroberylate (TGFBe; Hoshino *et al.*, 1957; Pepinsky *et al.*, 1957). The triglycine sulfophosphate (TGSP) crystal, which has a critical phase-transition temperature T_c of 324 K (Ravi *et al.*, 1993), can be used in the fabrication of pyroelectric devices (Ravi *et al.*, 1994). The phosphites show great industrial importance. For example, they are used as stabilisers for polyvinyl chloride and other polymers. When used with other stabilizing ingredients, they prevent the discoloration of the polymers by heat or UV light (Baran *et al.*, 1997).

The amino acid–phosphorous acid (H_3PO_3) composite crystal family also shows interesting dielectric and elastic properties; betainium phosphite (BPI) being a well known ferroelectric compound (Baran *et al.*, 1997). It undergoes a *para*-ferroelastic second-order phase transition at T_{c1} = 355 K and a *para*-ferroelectric phase transition at T_{c2} = 216 K. The glycinium phosphite (GPI) is another ferroelectric crystal which undergoes a continuous ferroelectric phase transition at T_c = 224 K (Albers *et al.*, 1988). Their crystal structures are built of amino acid layers which are held together by strong hydrogen bonds to infinite chains of hydrogen-bonded phosphite anions. In GPI phosphite anions are hydrogen-bonded to

infinite chains directed along the crystallographic *c*-axis (Averbuch-Pouchot, 1993*a*). The mechanism of the ferroelectric phase transition in GPI is connected to a dynamical disorder of the protons in the interphosphite hydrogen bonds, which is coupled to the motions of the ammonium groups of glycinium cations (Tritt-Goc *et al.*, 1998; Morawski *et al.*, 1998), whereas in BPI the phosphite anions are joined by hydrogen bonds in a dimer fashion into infinite chains along the ferroelectric *b* axis. Such an arrangement of protons in the hydrogen-bonded anions of the betainium phosphite crystal is related to the ferroelectricity observed in this compound

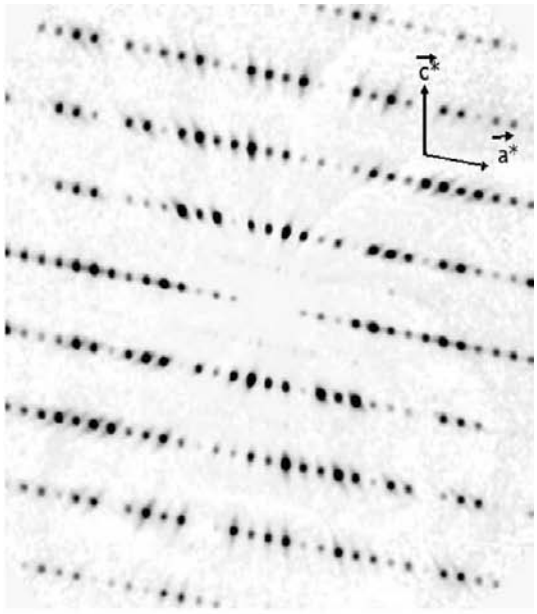

(*a*)

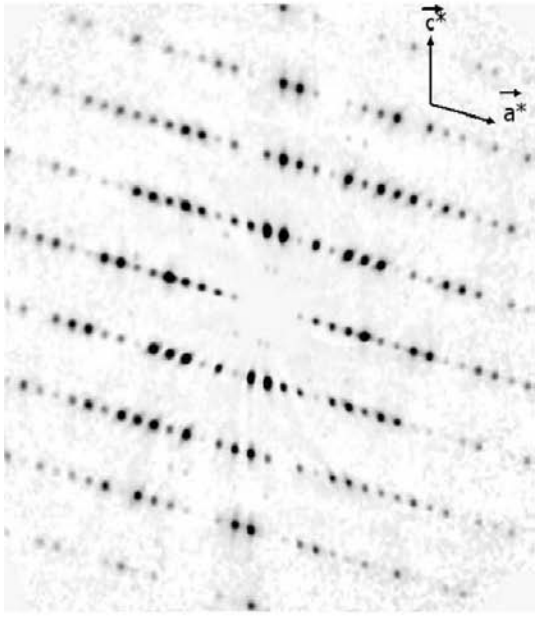

(*b*)

Figure 1
Diffractograms from (*h*0*l*)* reciprocal plane: (*a*) at 100 K; (*b*) at 293 K.

(Fehst *et al.*, 1993). The phosphite tetrahedra connect together in various ways to form inorganic networks, which may be zero- (*i.e.* dimer or cluster), one-, two- or three-dimensional in nature. As observed in 2-amino-5-nitropyridinium hydrogenphosphite (Pecaut & Bagieu-Beucher, 1993), anilinium hydrogenphosphite (Paixão, Matos Beja, Ramos Silva & Martin-Gil, 2000), 3-ammonium propanoic acid monohydrogenphosphite (Averbuch-Pouchot, 1993*b*) and diphenylguanidinium monohydrogenphosphite phosphorous–acid-water (Paixão, Matos Beja, Ramos Silva & Alte da Veiga, 2000), the phosphite groups are hydrogen-bonded in pairs (clusters). In other organic phosphite examples (Averbuch-Pouchot, 1993*a*,*c*,*d*,*e*; Fleck *et al.*, 2000; Paixão *et al.*, 2001; Harrison, 2003*a*,*b*,*c*; Mahmoudkhani & Langer, 2001; Harrison, 2004) the phosphite monoanions are linked to form infinite chains, whereas in some organic compounds (Averbuch-Pouchot, 1993*f*; Idrissi *et al.*, 2002; Bendheif *et al.*, 2003; Gordon & Harrison, 2003) the monoanions are not held together, *i.e.* no hydrogen bonding occurs between $H_2PO_3^-$ anions.

On the other hand, hydrogen bonds that could be expected in these salt crystals play an important role in many biochemical mechanisms. Indeed, the hydrogen-bonding geometries involving phosphate groups indicate that P—O···H—O—P and P—O···H—N bonds are generally the strongest O···O and O···N bonds that arise in biochemical systems. In particular, the strong effects of hydrogen bonding and proton transfer on P—O bond strengths are probably important for activating reactants and stabilizing intermediates in the reactions of the ATP-ADP biochemical energy cycle (Blessing, 1986).

Within a systematic investigation of new hybrid materials resulting from the association of amino acids with phosphorous acid, we report in this work on the synthesis, differential scanning calorimetry (DSC) measurements, cell-temperature dependence parameters and accurate X-ray diffraction of the *m*-carboxyphenylammonium monohydrogenphosphite, $C_7H_8NO_2^+\cdot PO_3^-$ (hereafter abbreviated to *m*-CPAMP) at low- and high-temperature phases (LTP) and (HTP), respectively.

2. Experimental

2.1. Syntheses

Crystals of *m*-CPAMP were obtained by mixing a solution of phosphorous acid (30%) with an aqueous solution of *m*-amino benzoic acid, $C_7H_8NO_2$, in stoichiometric ratios. The resulting aqueous solution was then kept at room temperature. After a few days of slow evaporation, large brown plate-shaped single crystals appeared in the solution.

2.2. Single-crystal X-ray diffraction

X-ray diffraction data on a crystal of 0.4 × 0.4 × 0.2 mm^3 were collected on an Oxford Xcalibur Sapphire2 CCD-based diffractometer with graphite-monochromated Mo $K\alpha$ radia-

Table 1
Main crystallographic features, X-ray diffraction data collection parameters and final results for $C_7H_8NO_2^+\cdot H_2PO_3^-$ at 100 and 293 K.

	100 K	293 K
Crystal data		
Chemical formula	$C_7H_8NO_2^+\cdot H_2PO_3^-$	$C_7H_8NO_2^+\cdot H_2PO_3^-$
M_r	219.13	219.13
Cell setting, space group	Monoclinic, $P2_1/c$	Monoclinic, $P2_1/c$
a, b, c (Å)	12.1405 (7), 12.4273 (9), 6.3851 (4)	13.036 (3), 11.538 (2), 6.6366 (13)
β (°)	100.122 (5)	104.73 (3)
V (Å^3)	948.35 (11)	965.4 (4)
Z	4	4
D_x (Mg m^{-3})	1.535	1.508
Radiation type	Mo $K\alpha$	Mo $K\alpha$
No. of reflections for cell parameters	9599	9599
θ range (°)	3.4–30.0	4.8–30.0
μ (mm^{-1})	0.29	0.28
Temperature (K)	100 (2)	293 (2)
Crystal form, colour	Plate, brown	Plate, brown
Crystal size (mm)	0.40 × 0.40 × 0.20	0.40 × 0.40 × 0.20
Data collection		
Diffractometer	Xcalibur-Saphire2	Xcalibur-Saphire2
Data collection method	ω	ω
Absorption correction	Integration	Integration
T_{min}	0.908	0.896
T_{max}	0.938	0.946
No. of measured, independent and observed reflections	78 938, 2751, 2731	26 411, 2807, 2063
Criterion for observed reflections	$I > 2\sigma(I)$	$I > 2\sigma(I)$
R_{int}	0.032	0.041
θ_{max} (°)	30.0	30.0
Range of h, k, l	$-17 \Rightarrow h \Rightarrow 16$ $0 \Rightarrow k \Rightarrow 17$ $0 \Rightarrow l \Rightarrow 8$	$-17 \Rightarrow h \Rightarrow 18$ $-16 \Rightarrow k \Rightarrow 0$ $-9 \Rightarrow l \Rightarrow 0$
Refinement		
Refinement on	F^2	F^2
$R[F^2 > 2\sigma(F^2)]$, $wR(F^2)$, S	0.035, 0.094, 1.08	0.037, 0.103, 0.99
No. of reflections	2751	2807
No. of parameters	165	165
H-atom treatment	Mixture of independent and constrained refinement	Mixture of independent and constrained refinement
Weighting scheme	$w = 1/[\sigma^2(F_o^2) + (0.0599P)^2 + 0.3946P]$, where $P = (F_o^2 + 2F_c^2)/3$	$w = 1/[\sigma^2(F_o^2) + (0.0639P)^2]$, where $P = (F_o^2 + 2F_c^2)/3$
$(\Delta/\sigma)_{max}$	0.026	<0.0001
$\Delta\rho_{max}$, $\Delta\rho_{min}$ (e Å^{-3})	0.56, −0.32	0.27, −0.34

Computer programs used: *CrysAlis CCD* and *CrysAlis RED* (Oxford Diffraction, 2004), *SHELXS*97 (Sheldrick, 1998), *SHELXL*97 (Sheldrick, 1998), *ORTEP*III (Farrugia, 1997), *WinGX* publication routines (Farrugia, 1999).

tion (λ = 0.71073 Å) equipped with a liquid-nitrogen Oxford Cryostream cooling device. The temperature control was calibrated using a K-type Chromel–Alumel thermocouple positioned at the same place as the crystal. The crystal temperature was stable to within 2 K. The crystal-to-detector distance was fixed at 40 mm. The cell parameters were determined from 320 to 100 K and from 100 to 320 K from the analysis of the Bragg peak positions collected on the same sets of 15 images by steps of 20 K from 100 to 210 K; the step size was reduced to 5 K in the 210–240 K and 250–270 K temperature ranges, whereas it was only 3 K around the transition.

2.3. Reciprocal space reconstruction

The reconstructed precession images reveal the presence of weak satellite reflections in the ($h0l$) reciprocal plane for both LTP and HTP (Fig. 1). However, only 37 and 18 satellites above the 2σ limit were detected at 100 and 293 K, respectively. The small number of observed satellite reflections and their weak intensities do not facilitate their analysis. Higher-intensity synchrotron radiation is necessary to record the satellite diffraction pattern that is required for accurate analysis and refinement of the modulated structure.

2.4. Structure refinements

For the structure refinements (100 and 293 K), X-ray diffraction data were collected at fixed detector positions using ω step scans repeated at eight different values of the φ angle. Each frame covered a 1° ω rotation step. The intensity decay was monitored by repeating the initial frames at the end of the data collections and analysing the duplicate reflections. Coverage of reciprocal space was more than 99% complete to $(\sin\theta/\lambda) = 0.7$ Å^{-1} with an average redundancy of 4. Data processing was performed using the *Crysalis-Red* program (Oxford Diffraction, 2004). Absorption effects were corrected by numerical methods based on crystal face indexing (using the program *ABSORB*; DeTitta, 1985). The structures were solved by direct methods (Sheldrick, 1998) and successive Fourier synthesis and then refined by full-matrix least-squares refinements on F^2. All calculations were carried out using the *WinGX* software package (Farrugia, 1999). The electron density of the H atoms was clearly identified in the difference Fourier maps and their atomic coordinates and isotropic displacement parameters were refined, except for the H atoms on the O1 and O5 atoms only positions were refined with $U_{iso}(H) = 1.5\,U_{eq}(O)$ at both 100 and 293 K. Crystallographic data and details of the data collection and refinement for 100 and 293 K are given in Table 1.[1]

[1] Supplementary data for this paper are available from the IUCr electronic archives (Reference: CK5008). Services for accessing these data are described at the back of the journal.

2.5. DSC measurements

DSC (differential scanning calorimetry) measurements were performed on heating and cooling *m*-CPAMP samples in the temperature range 173–373 K using a TC11 equipped with a modulate DSC 30 METTLER instrument in order to thermodynamically quantify the phase transition observed from X-ray data (see below). The measurements were carried out under argon at atmospheric pressure in aluminium crucibles with a heating rate of 1 K min^{-1}.

3. Results and discussion

3.1. Temperature-induced phase transition

3.1.1. Differential scanning calorimetry. The calorimetric behaviour of *m*-CPAMP was studied by measuring the enthalpy with differential scanning calorimetry (Fig. 2). Upon heating and cooling 30.4 mg of the sample in the 173–373 K temperature range, the crystalline substance undergoes a single phase transition at *ca* T_c = 246 (2) K. DSC scans of a sample that had been repeatedly cooled and heated several times showed an exothermic peak at 246.0 K with an enthalpy of 1.300 kJ mol^{-1} and an endothermic peak at 249.6 K with an enthalpy of 1.346 kJ mol^{-1}. The observed peaks represent a reversible phase transition with a 3.6 K hysteresis between the phase transformation temperatures. This thermal hysteresis is indicative of a first-order phase transition.

3.1.2. The modulated structure. Owing to the very low intensities of the satellite reflections, it was very difficult to refine the modulation wavevector **q**. The best estimates of the **q** vector at 100 and 293 K using the program *NADA* (Schönleber *et al.*, 2001) are

$$\mathbf{q}_{100} \simeq 0.24\,(3)\mathbf{a}^* + 0.49\,(3)\mathbf{b}^* + 0.48\,(4)\mathbf{c}^*,$$
$$\mathbf{q}_{293} \simeq 0.25\,(2)\mathbf{a}^* + 0.49\,(6)\mathbf{b}^* + 0.49\,(6)\mathbf{c}^*.$$

The weakness and the small number of satellite reflections observed on the laboratory diffractometer (Fig. 1) does not allow a more accurate determination. The question of whether the modulation is commensurate or incommensurate can only be answered with synchrotron diffraction data which we plan to collect in the near future. Therefore, this paper will describe the phase transition by analysing only the average structures and cell parameter dependence using the main reflections.

3.1.3. Thermal evolution of the lattice parameters. Fig. 3 displays the evolution of the cell parameters as a function of temperature. All cell parameters display an abrupt jump at T_c = 246 (2) K, as expected from the DSC measurements. When the phase transition takes place, the *b* cell parameter strongly decreases with increasing temperature and remains relatively constant above T_c, whereas the *a* and *c* cell parameters increase with increasing temperature. All parameters present an abrupt jump at T_c, which is more pronounced for *a* and *b* ($\Delta a/a = 6.87\%$ and $\Delta b/b = -7.7\%$) than for *c* ($\Delta c/c = 3.8\%$). The β angle also undergoes a significant temperature-dependent variation changing from 100.122 (5) to 104.73 (3)° corresponding to $\Delta\beta/\beta = 4.4\%$ at T_c. The volume variation is about $\Delta V/V = 1.77\%$ with a molar volume discontinuity at T_c. This behaviour reveals the three-dimensional nature of the interactions. The hysteresis also clearly shows up on the thermal behaviour of the unit-cell parameters: as an example Fig. 4 shows that the hysteresis range is 3 (± 0.3) K, in excellent agreement with the DSC measurements.

3.1.4. Principal linear thermal expansion/contraction. Distortion of a crystal structure can be characterized by the overall change in molar volume or, in other terms, by a mean volume expansion (contraction) coefficient, as calculated from

$$\alpha_T = 1/V_0 \Delta V/\Delta T.$$

This is, however, not a very good criterion since the distortion of a crystal is anisotropic, *i.e.* the linear strain (expansion or contraction) depends on the direction. The principal linear thermal expansion/contraction coefficient along a given crystallographic *a* axis is defined as

$$\alpha_a = 1/(a_{293}).\mu_a,$$

where $\mu_a = (\delta a)/(\delta T)$ is the slope of the *a versus T* plot, calculated

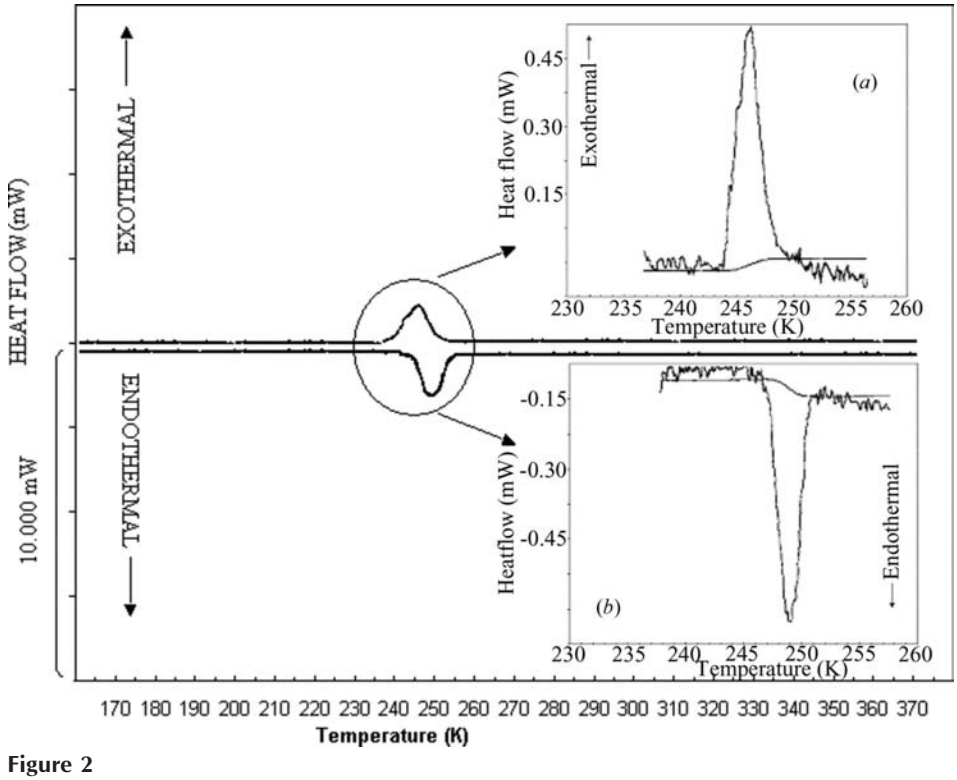

Figure 2
Differential scanning calorimetry (DSC) thermograph of *m*-CPAMP: (*a*) cooling; (*b*) heating.

from the measured changes in lattice parameters with temperature (Fig. 3) using the following linear equations (Nye, 1994)

$$a = \mu_a T + a_0,$$

where a_0 is the unit-cell parameter value at 0 K. The principal linear thermal expansion/contraction coefficients along the crystallographic axes calculated for the low-temperature (LTP) and high-temperature (HTP) phases are summarized in Table 2. These values reveal that the linear thermal expansion/contraction, along the *a* axis (α_a) decreases from 7.67 to 2.30 × 10^{-5} K^{-1} when the crystal undergoes the phase transition on heating, whereas α_b increases (three times) from 4.33 to 13 × 10^{-5} K^{-1} in absolute values. The axial thermal expansion/contraction along the *c* axis (α_c) remains almost invariant in both LTP and HTP phases.

3.2. Average low-temperature structure and crystal packing

The room-temperature crystal structure of *m*-CPAMP was recently determined by Benali–Cherif and coworkers (Benali-Cherif *et al.*, 2004). The average low-temperature phase (LTP;

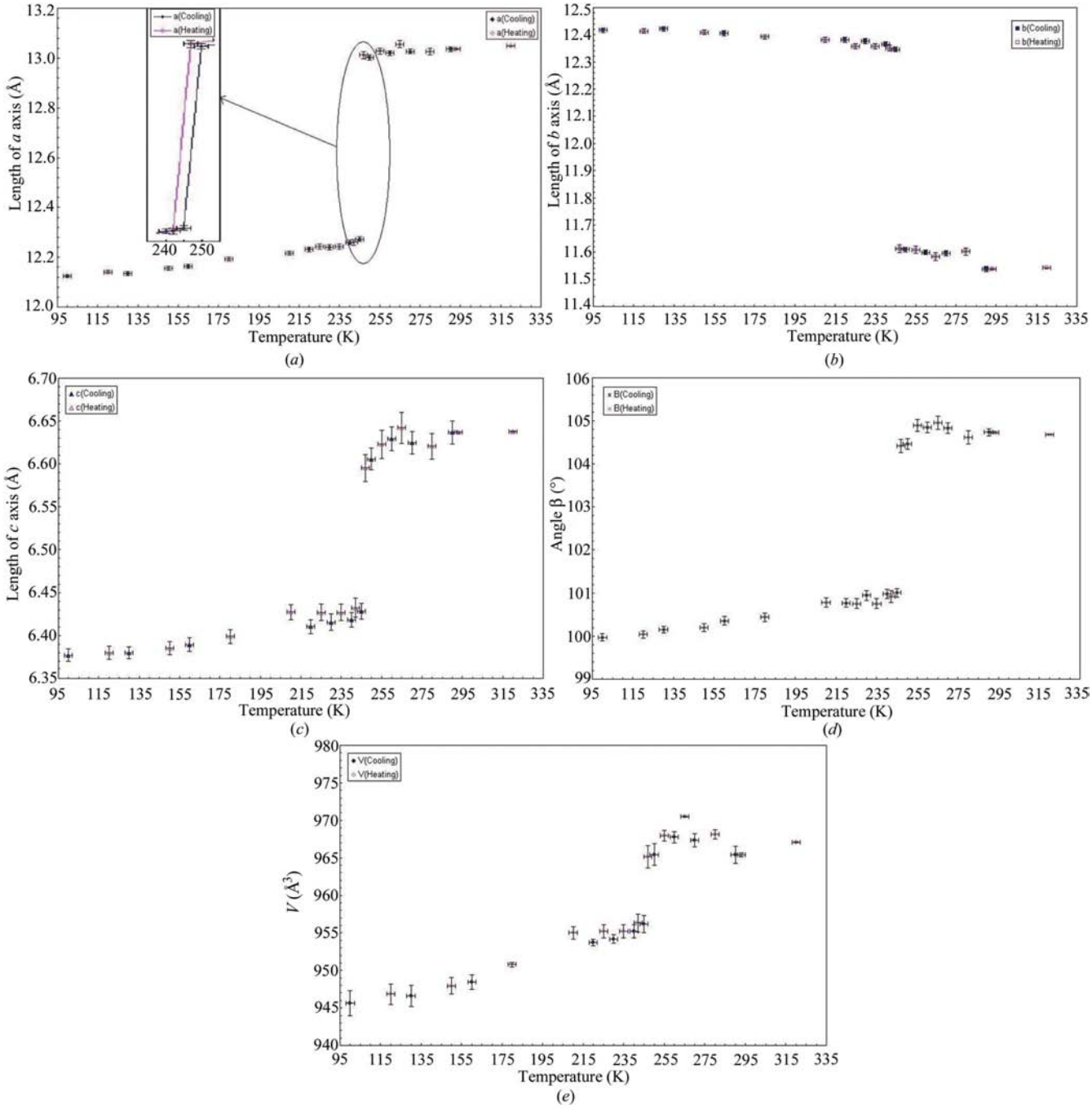

Figure 3
Temperature dependence of the unit-cell parameters and volume; the temperature error bar is the estimated absolute error (±2 K).

Table 2
Principal linear thermal expansion/contraction coefficients.

Unit-cell parameter	Coefficient	LTP	HTP
	a_0 (Å)	12.01	12.957
a	$\mu_a \times 10^{-4}$ (Å K^{-1})	10	3
	$\alpha_a \times 10^{-5}$ (K^{-1})	7.67	2.30
	b_0 (Å)	12.48	11.979
b	$\mu_b \times 10^{-4}$ (Å K^{-1})	−5	−15
	$\alpha_b \times 10^{-5}$ (K^{-1})	−4.33	−13
	c_0 (Å)	6.33	6.51
c	$\mu_c \times 10^{-4}$ (Å K^{-1})	4	4
	$\alpha_c \times 10^{-5}$ (K^{-1})	6.03	6.03

Fig. 5) also belongs to the monoclinic centrosymmetric space group $P2_1/c$, with one monohydrogenphosphite anion and one *m*-carboxyphenyl ammonium cation in general positions (Fig. 6) in the asymmetric unit. Therefore, the phase transformation does not induce any change in the crystal symmetry. In order to understand the structure changes of the two phases, the room-temperature structure has been remeasured to have a similar accuracy of the bond lengths and angles for both temperatures.

There is a very close resemblance between the two average crystal structures phases. Both ionic structures can be described as alternating layers of HPO_3H^- anions and $NH_3C_6H_4COOH^+$ cations perpendicular to the [001] direction (Fig. 6). The arrangement is characterized by centrosymmetric $H_4P_2O_6^{2-}$ dimers and the crystal is stabilized by a three-dimensional network of hydrogen bonds which are held together as both anionic dimers and cationic layers.

The geometry of the inorganic moiety is usual. The P atoms are tetrahedrally coordinated by one H and three O atoms. Inspection of the distorted tetrahedral geometry of the monohydrogenphosphite anion at 100 K (see Table 3) shows that the two P—O(T) bonds corresponding to the terminal O atoms (O3 and O4) are identical within 1 s.u. [1.5157 (7) and 1.5165 (8) Å] as a result of the delocalization of the negative charge between them, and are significantly shorter than the protonated P—O5 bond [1.5711 (8) Å]. The O—P—O angle corresponding to the shortest P—O distances is 116.08 (4)°, whereas the mean value of the O—P—OH angles is 109.81 (4)°. This is induced by the mutual repulsion of the nonbridging O atoms. These bond lengths and angles are in good agreement with those observed in similar compounds (Pecaut & Bagieu-Beucher, 1993; Paixão, Matos Beja, Ramos Silva & Martin-Gil, 2000; Paixão, Matos Beja, Ramos Silva & Alte da Veiga, 2000; Averbuch-Pouchot, 1993*b*).

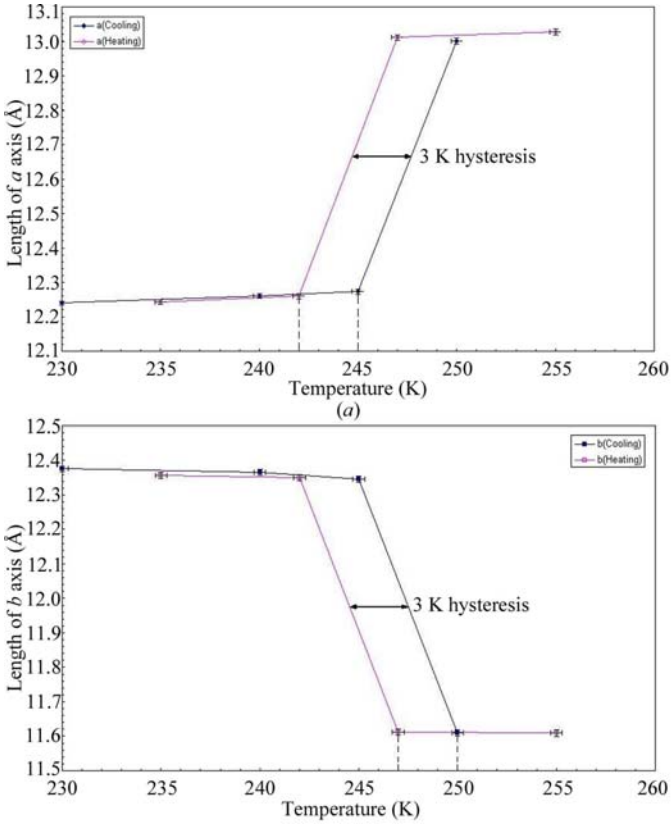

Figure 4
Phase transition hysteresis as revealed by the behaviour of the *a* and *b* parameters behaviour; the relative temperature error bar is estimated from the stability of the temperature (±0.3 K).

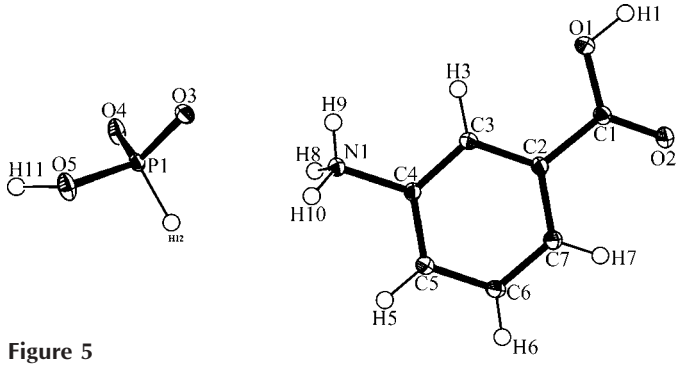

Figure 5
A perspective view of the *m*-carboxyphenylammonium monohydrogenphosphite at 100 K (*ORTEP*3; Farrugia, 1997) with the atom-labelling scheme. Thermal displacement ellipsoids are drawn at the 50% probability level. H atoms are represented by spheres.

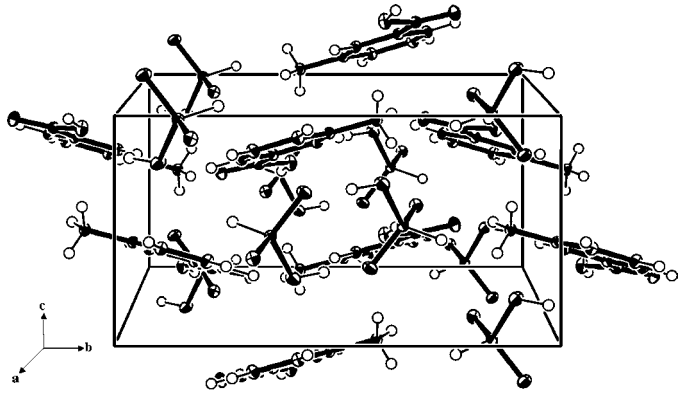

Figure 6
Unit-cell projection on the (100) plane at 100 K of the packing of $C_7H_8NO_2^+$, $H_2PO_3^-$ showing the alternating $C_7H_8NO_2^+$ and $H_2PO_3^-$ moieties.

Table 3
Geometry of the inorganic anion in HTP and LTP.

The three P—O distances and the P—H distance are in the diagonal of the table. The three O—P—O angles and the three O—P—H angles are below the diagonal. The five internal O···O distances as well as the O···H distance are above the diagonal.

100 K (LTP)				
P1	O3	O4	O5	H12
O3	*1.5157 (7)*	2.5724 (11)	2.4967 (11)	2.2933 (16)
O4	116.08 (4)	*1.5165 (8)*	2.5548 (11)	2.2773 (16)
O5	107.94 (4)	111.67 (4)	*1.5711 (8)*	2.2855 (16)
H12	108.3 (7)	107.6 (7)	104.6 (7)	*1.307 (16)*
293 K (HTP)				
P1	O3	O4	O5	H12
O3	*1.4931 (11)*	2.5589 (15)	2.4467 (16)	2.2297 (16)
O4	117.79 (7)	*1.4954 (11)*	2.5205 (14)	2.2518 (16)
O5	106.46 (7)	111.16 (7)	*1.5593 (12)*	2.2441 (16)
H12	107.3 (7)	108.8 (7)	104.5 (7)	*1.253 (16)*

Within organic cations the phenyl ring atoms are closely coplanar with C—C distances and C—C—C bond angles lying within the ranges 1.3914 (13)–1.4057 (13) Å and 118.28 (9)–121.94 (9)°, respectively. The carboxylic group is not deprotonated and the C1 atom has a slightly distorted sp^2 environment revealed by C=O and C—OH bond lengths of 1.2303 (12) and 1.3236 (12) Å, respectively, and by O1—C1—O2 bond angles of 123.87 (9)° (see Table 4 for details). The environment around the N atom is tetrahedraly distorted. Moreover, the $C_{ar}—NH_3^+$ bond is longer than the corresponding $C_{ar}—NH_2$ bond and the endocyclic angle to the *meta* substituent, C3—C4—C5, is larger than 120° [121.94 (9)°], as predicted by charge consideration. This reveals a decrease of the π bond character in $C_{ar}—NH_3^+$ due to the protonation of the amino group occurring in the reaction with phosphorous acid. The mean deviation of the ammonium exocyclic group from the least-squares plane of the phenyl ring is very small [−0.0178 (9) Å] and corresponds to a (1°) out-of-plane bending of the C4—N1 bond. The ammonium NH_3^+ group is slightly staggered from the plane of the benzene ring; this staggered conformation was found in a number of *m*-carboxyphenylammonium salts (Benali-Cherif *et al.*, 2002; Bendjeddou *et al.*, 2003) and it appears to be preferred over the eclipsed conformation observed previously in *m*-carboxyphenylammonium bisulfate (Cherouana *et al.*, 2003). The geometrical features of the *m*-carboxyphenylammonium cations are also in accordance with other similar compounds (see, for example, Arora *et al.*, 1973).

The HPO_3H^- tetrahedra are held together in pairs by strong O4···H11—O5 hydrogen bonds, yielding $(H_4P_2O_6)^{2-}$ clusters in the structure: the resulting short O4···O5 distances [2.5456 (11) Å] as well as the internal P···P distance [4.274 (2) Å] between the HPO_3H^- units compare well with those found in other dimers (Pecaut & Bagieu-Beucher, 1993; Paixão, Matos Beja, Ramos Silva & Martin-Gil, 2000; Paixão, Matos Beja, Ramos Silva & Alte da Veiga, 2000; Averbuch-Pouchot, 1993*b*).

The *m*-carboxyphenyl ammonium cations are arranged in zigzag layers along the *b* axis, sandwiched between the phosphoric macroanions dimers (Fig. 7). The organic cations are joined together *via* only one hydrogen bond from the ammonium group toward the carboxylic group. This arrangement gives rise to a three-dimensional network in which the O atoms of monohydrogenphosphite anions act as proton acceptors or as proton donors. Both O3 and O4 atoms are bifurcated acceptors of hydrogen bonds, while O5 acts as a hydrogen-bond donor (see Table 5). Hence, the ammonium group *via* its two H atoms (H8 and H10) serves as a hydrogen-

Table 4
Geometry (Å, °) of the organic cation.

T (K)	100	293
Carboxylic group		
C1—O1	1.3236 (12)	1.3130 (16)
C1—O2	1.2303 (12)	1.2169 (16)
C1—C2	1.4945 (13)	1.4905 (18)
O1—C1—O2	123.87 (9)	123.71 (13)
O2—C1—C2	121.60 (9)	121.38 (12)
O1—C1—C2	114.52 (8)	114.49 (11)
C1—C2—C7	118.14 (8)	119.24 (12)
C1—C2—C3	121.36 (8)	120.41 (11)
O2—C1—C2—C7	−4.22 (14)	1.4 (2)
O1—C1—C2—C7	174.61 (9)	−179.99 (12)
O2—C1—C2—C3	175.79 (9)	−177.61 (14)
O1—C1—C2—C3	−5.38 (14)	1.0 (2)
Ammonium group		
C4—N1	1.4668 (12)	1.4657 (17)
C3—C4—N1	119.74 (8)	119.12 (11)
C5—C4—N1	118.29 (8)	119.60 (12)
Phenyl ring		
C2—C3	1.4057 (13)	1.3855 (18)
C2—C7	1.4002 (13)	1.3938 (18)
C3—C4	1.3914 (13)	1.3823 (18)
C4—C5	1.3959 (13)	1.3894 (18)
C5—C6	1.3941 (14)	1.384 (2)
C6—C7	1.3980 (13)	1.378 (2)
Mean (C—C) (Å)	1.3976 (13)	1.3855 (15)
C7—C2—C3	120.49 (9)	120.34 (12)
C2—C3—C4	118.28 (9)	118.96 (12)
C3—C4—C5	121.94 (9)	121.27 (12)
C4—C5—C6	119.22 (9)	119.04 (13)
C5—C6—C7	120.05 (9)	120.57 (13)
C6—C7—C2	120.00 (9)	119.80 (13)

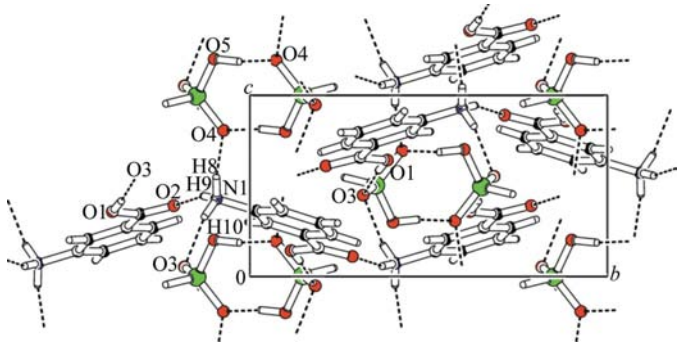

Figure 7
PLATON (Spek, 2003) projection on the (100) plane of the hydrogen-bonding network at 100 K.

bond donor to two different HPO_3H^- anions belonging to two different $H_4P_2O_6^{2-}$ dimers [N1···O4 = 2.7966 (12) and N1···O3 = 2.8096 (12) Å]. This gives rise to the formation of $C_2^2(5)$ hydrogen-bonded chains (hydrogen-bond graph-set notation; Bernstein *et al.*, 1995; Fig. 6), while the H9 atom of the NH_3^+ group interacts with the carboxyl O2 atom of the adjacent organic group [N1···O2 = 2.8097 (12) Å], yielding the organic cation layers. The last hydrogen bond involves the H atom of the hydroxyl group of the organic cations and establishes a connection with a third HPO_3H^- anion [O1···O3 = 2.5977 (11) Å]. The hydrogen bond between the carboxylic group and the monohydrogenphosphite anions appears to be shorter than those observed between the ammonium group and the monohydrogenphosphite anions. As expected, the phosphite H atom (P—H) is not involved in the hydrogen-bonding scheme.

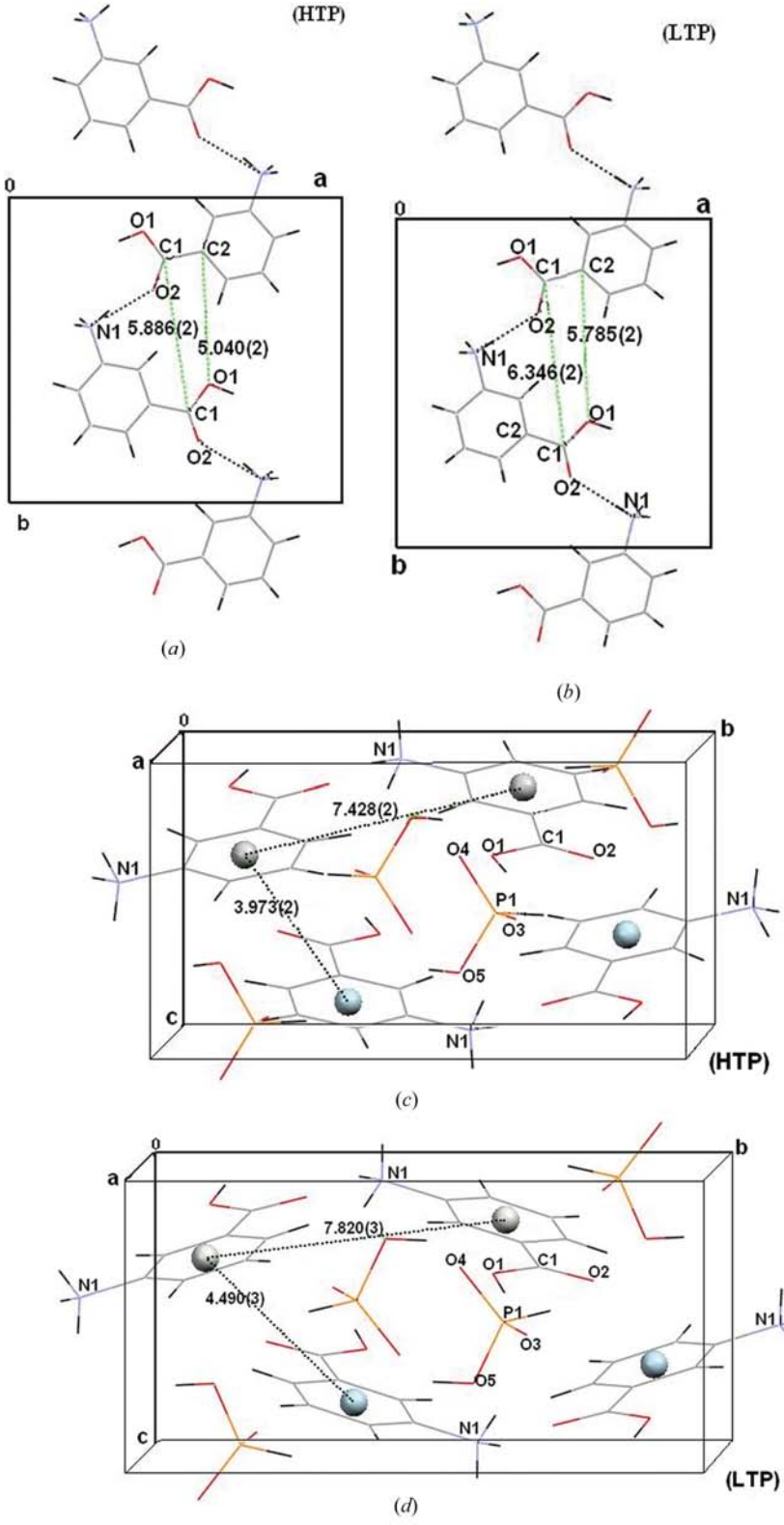

Figure 8
Intermolecular distance changes with temperature: (*a*) viewed down the *c* axis (phosphite anions have been removed for clarity); (*b*) viewed down the *a* axis.

3.3. Phase transition mechanism

A precise analysis of the (LTP) structure is needed to discover the important packing and structural differences compared with (HTP). The behaviour of both ions with temperature shows that the phosphite macroanions and organic cations mostly act as rigid groups. The signature of the transition from the low-temperature phase to the high-temperature phase is a significant reorganization of the molecular packing, characterized by a shift of the alternating organic cations and phosphite anions. With increasing temperature, the organic cations belonging to the same layer approach each other along the *b* direction; this results in a significant shortening of the O1···C2′ and C1···C1′ intermolecular distances (which are approximately parallel to the *b* axis) by 0.745 and 0.460 Å, respectively (Figs. 8*a* and *b*). On the other hand, Figs. 8(*c*) and (*d*) show that the separation between the centroids of two neighbouring phenyl rings of one layer [7.820 (3) Å at 100 K] decreases to 7.428 (2) Å at 293 K as well as the centroids's separation between layers related *via* HPO_3H^- anions [4.490 (3) Å at 100 K to 3.973 (2) Å at 293 K].

These molecular movements along the *b* axis induce a steric effect, which forces the anions and carbocations to rotate around the *b* axis by *ca* 4.6° in the *ac* plane (Fig. 9). Consequently, the strength of the weakest hydrogen bond approximately parallel to the *c* axis decreases, as shown by the large increase of the N1···O3

distance [from 2.8096 (12) to 2.8740 (18) Å]. This explains the unit-cell parameter changes with temperature: indeed, when the temperature increases the translation of both ions along the *b* axis induces a reduction in the *b* parameter, whereas the *a*, *c* and β parameters increase as a consequence of the 4.6° rotation of both ions around the *b* axis in the *ac* plane.

Such large changes in the parameters surprisingly cause only small, but significant, differences in the molecular conformation: the HPO_3H^- tetrahedra become slightly stretched at low temperature, as reflected in the increase of bond lengths and the decrease in tetrahedral angles (Table 3). The phase transition is also associated with a small phenyl ring distortion (Table 4). The shifts in the average C—C distances and C—C—C bond angles are *ca* 0.0121 Å and 0.46°, respectively. The C—OH and C=O distances also decrease slightly from 1.3236 (12) to 1.3130 (16) Å and from 1.2303 (12) to 1.2169 (16)°, respectively; the O1—C1—O2 bond angles vary from 123.87 (9) to 123.71 (13)° with increasing temperature. The carboxylic group is twisted from the plane of the phenyl ring by 5.38° at 100 K and 3.04° at 293 K, the carboxylic C1 atom is displaced from the mean planes of the phenyl ring by −0.0475 (13) Å at 293 K and by only −0.0119 (9) Å at 100 K. The carboxyl O2 atom is displaced from the benzene ring by −0.0972 (12) and 0.0667 (8) Å at 293 and 100 K, respectively, while the O1 atom is displaced from the mean planes of the phenyl ring by −0.0548 (11) and −0.1347 (8) Å at 293 and 100 K, respectively. These deviations are due to the rotation of the carboxylic group around the C1—C2 bond, as indicated by the important changes in the O1—C1—C2—C3 and O1—C1—C2—C7 torsion angles which vary from −5.38 (14) to 1.0 (2)° and from 174.61 (9) to −179.99 (12)°, respectively. The C1—C2 bond shows an out-of-plane bending of 1.61° at 293 K and only 0.35° at 100 K (see Table 4 for more details).

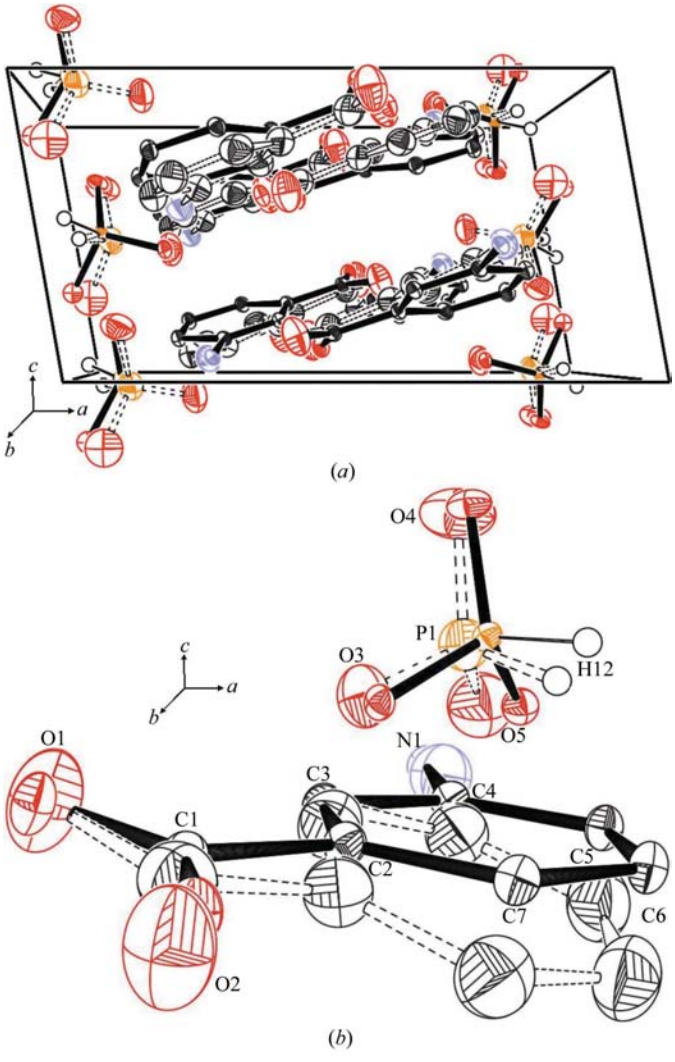

Figure 9
View of the molecular change *versus* temperature. The HTP phase is represented by dashed lines.

Table 5
Hydrogen-bonding geometry (Å, °).

D···H···*A*	*D*—H	H···*A*	*D*···*A*	*D*—H···*A*
LTP O5···H11···O4^{i}	0.979 (19)	1.570 (19)	2.5456 (11)	173.4 (18)
HTP O5···H11···O4^{i}	0.86 (3)	1.71 (3)	2.5590 (19)	168 (3)
LTP O1···H1···O3^{ii}	0.901 (17)	1.702 (18)	2.5977 (11)	172.3 (18)
HTP O1···H1···O3^{ii}	0.85 (2)	1.78 (3)	2.5982 (16)	161.1 (19)
LTP N1···H8···O4^{iii}	0.895 (19)	1.909 (19)	2.7966 (12)	170.9 (18)
HTP N1···H8···O4^{iii}	0.917 (19)	1.860 (19)	2.7693 (17)	170.9 (16)
LTP N1···H9···O2^{iv}	0.850 (19)	1.982 (19)	2.8097 (12)	164.5 (18)
HTP N1···H9···O2^{iv}	0.96 (2)	1.84 (3)	2.7865 (17)	166 (2)
LTP N1···H10···O3^{v}	0.879 (18)	1.961 (19)	2.8096 (12)	161.8 (17)
HTP N1···H10···O3^{v}	0.97 (3)	1.94 (3)	2.8740 (18)	159 (2)

Symmetry codes: (i) $-x, -y, -z$; (ii) $1-x, \frac{1}{2}+y, \frac{1}{2}-z$; (iii) $x, \frac{1}{2}-y, z-\frac{1}{2}$; (iv) $1-x, y-\frac{1}{2}, \frac{1}{2}-z$; (v) $x, \frac{1}{2}-y, \frac{1}{2}+z$.

Notwithstanding the molecular rearrangement, the other intermolecular contacts through hydrogen bonding remain surprisingly similar. Hence, both inter-anion (O4···O5) and carboxy–phosphite (O1···O3) interactions show only slight variations, 0.0134 (16) and 0.0005 (14) Å, respectively. The interactions involving the ammonium group (N1···O2 and N1···O4) only decrease by 0.0253 (15) Å with increasing temperature from 100 to 293 K.

These variations are related to the small enthalpy required for the structural transition as observed above by DSC measurements: in fact, it mostly concerns the weakest N1···O3 hydrogen bond.

4. Conclusion

This paper is a first attempt to describe the phase transition of (*m*-CPAMP) using only the accurate main X-ray reflections: this compound undergoes a reversible phase transition as evidenced by the behaviour of the unit-cell parameters *versus* temperature and by differential scanning calorimetry measurements. On heating and cooling the *m*-CPAMP sample in the 100–320 K temperature range, the phase transition occurs at *ca* T_c = 246 (2) K. The reported phase transition appears to be first order according to the thermal hysteresis, 3.6 K, and the observed abrupt jumps of the unit-cell para-

meters with temperature which also confirmed the hysteresis. Between 100 and 320 K the transition may be globally described at the molecular level by the rotation of both cations and anions by *ca* 4.6° around the crystallographic *b* axis induced by their translation along the *b* direction. The phase transition only causes a slight distortion of the HPO_3H^- tetrahedral geometry as well as for organic cations.

Owing to the complexity of the phase transition, the measurements of the satellite reflections on synchrotron as well as neutron single-crystal diffraction are necessary. Owing to the weak neutron–matter interaction, it is likely that the satellite reflections cannot be measured accurately but the main reflections will allow a TLS description using the H atom owing to the weak neutron–matter interaction. The latter are necessary for a total interpretation of the phase transition.

The authors would like to thank the service Commun de Diffraction X sur Monocristaux (Université Henri Poincaré, Nancy 1) for providing access to crystallographic experimental facilities. Authors are very grateful to A. Bouché and E. Wenger for their technical assistance. We also thank one referee for stimulating comments. E. Bendeif is grateful to l'Agence Universitaire de la Francophonie (AUF) for financial support (Imputation coda: 1021FR412L).

References

Albers, J., Klopperpieper, A., Rother, H. J. & Haussuhl, S. (1988). *Ferroelectrics*, **81**, 27.
Arora, S. K., Sundaralingam, M., Dancz, J. S., Stanford, R. H. & Marsh, R. E. (1973). *Acta Cryst.* B**29**, 1849–1855.
Averbuch-Pouchot, M. T. (1993*a*). *Acta Cryst* C**49**, 815–818.
Averbuch-Pouchot, M. T. (1993*b*). *Z. Kristallogr.* **208**, 257–258.
Averbuch-Pouchot, M. T. (1993*c*). *Acta Cryst.* C**49**, 813–815.
Averbuch-Pouchot, M. T. (1993*d*). *Z. Kristallogr.* **208**, 366–367.
Averbuch-Pouchot, M. T. (1993*e*). *Z. Kristallogr.* **207**, 149–150.
Averbuch-Pouchot, M. T. (1993*f*). *Z. Kristallogr.* **207**, 111–120.
Baran, J., Czapla, Z., Drozd, M. K., Ilczyszyn, M. M., Marchewka, M. & Ratajczak, H. (1997). *J. Mol. Struct.* **403**, 17–37.
Benali-Cherif, N., Bendheif, L., Bouchouit, K., Cherouana, A., Bendjeddou, L. & Merazig, H. (2004). *Ann. Chim. Sci. Mater.* **292**, 11–24.
Benali-Cherif, N., Cherouana, A., Bendjeddou, L., Merazig, H., Bendheif, L. & Bouchouit, K. (2002). *Acta Cryst.* E**58**, o156–o157.
Bendjeddou, L., Cherouana, A., Berrah, F. & Benali-Cherif, N. (2003). *Acta Cryst.* E**59**, o574–o576.
Bendheif, L., Benali-Cherif, N., Benguedouar, L., Bouchouit, K. & Merazig, H. (2003). *Acta Cryst.* E**59**, o141–o142.
Bernstein, J., Davis, R. E., Shimoni, L. & Chang, N. L. (1995). *Angew. Chem. Int. Ed. Engl.* **34**, 1555–1573.
Blessing, R. H. (1986). *Acta Cryst.* B**42**, 613–621.
Cherouana, A., Bendjeddou, L. & Benali-Cherif, N. (2003). *Acta Cryst.* E**59**, o1790–o1792.
DeTitta, G. T. (1985). *J. Appl. Cryst.* **18**, 75–79.
Farrugia, L. J. (1997). *J. Appl. Cryst.* **30**, 565–566.
Farrugia, L. J. (1999). *J. Appl. Cryst.* **32**, 837–838.
Fehst, I., Paasch, M., Hutton, S. L., Braune, M., Brohmer, R., Loidl, A., Dorffer, R., Narz, T., Haussuhl, S. & Mclntyre, G. J. (1993). *Ferroelectrics*, **138**, 1–10.
Fleck, M., Tillmanns, E. & Haussuhl, S. (2000). *Z. Kristallogr. NCS*, **215**, 109–110.
Gordon, L. E. & Harrison, W. T. A. (2003). *Acta Cryst.* E**59**, o195–o197.
Harrison, W. T. A. (2003*a*). *Acta Cryst.* E**59**, o1351–o1353.
Harrison, W. T. A. (2003*b*). *Acta Cryst.* E**59**, o1267–o1269.
Harrison, W. T. A. (2003*c*). *Acta Cryst.* E**59**, o769–o770.
Harrison, W. T. A. (2004). *Acta Cryst.* E**60**, o1577–o1579.
Hoshino, S., Mitsui, T., Jona, F. & Pepinsly, R. (1957). *Phys. Rev.* **107**, 1255–1258.
Idrissi, A. K., Saadi, M., Rafiq, M. & Holt, E. M. (2002). *Acta Cryst.* C**58**, o604–o605.
Mahmoudkhani, A. H. & Langer, V. (2001). *Acta Cryst.* E**57**, o866–o868.
Matthias, B. T., Miller, C. E. & Remeika, J. P. (1956). *Phys. Rev.* **104**, 849–850.
Morawski, P., Gramza, M., Goslar, M., Hilczer, W., Szczepañska, L. & Hoffmann, S. K. (1998). *Ferroelectr. Lett.* **23**, 121.
Nye, J. (1994). *Physical Properties of Crystals. Their Representation by Tensors and Matrices*. Oxford University Press.
Oxford Diffraction (2004). *CrysAlis CCD and CrysAlis RED*. Oxford Diffraction Ltd, Abingdon, Oxfordshire, England.
Paixão, J. A., Matos Beja, A., Ramos Silva, M. & Martin-Gil, J. (2000). *Acta Cryst.* C**56**, 1132–1135.
Paixão, J. A., Matos Beja, A., Ramos Silva, M. & Alte da Veiga, L. (2000). *Z. Kristallogr. NCS*, **215**, 352–354.
Paixão, J. A., Matos Beja, A., Ramos Silva, M. & Alte da Veiga, L. (2001). *Z. Kristallogr. NCS*, **216**, 416–418.
Pecaut, J. & Bagieu-Beucher, M. (1993). *Acta Cryst.* C**49**, 834–837.
Pepinsky, R., Okaya, Y. & Jona, F. (1957). *Bull. Am. Phys. Soc.* **2**, 1538–1539.
Ravi, G., Anbukumar, S. & Ramasamy, P. (1993). *J. Cryst. Growth*, **133**, 212–216.
Ravi, G., Anbukumar, S. & Ramasamy, P. (1994). *Mater. Chem. Phys.* **37**, 180–183.
Schönleber, A., Meyer, M. & Chapuis, G. (2001). *J. Appl. Cryst.* **34**, 777–779.
Sheldrick, G. M. (1998). *SHELX*97 (includes *SHELXS*97 and *SHELXL*97, Release 97-2. University of Göttingen, Germany.
Spek, A. L. (2003). *J. Appl. Cryst.* **36**, 7–13.
Tritt-Goc, J., Pislewski, N., Szczepanskaa, L. & Gocb, R. (1998). *Solid State Commun.* **108**, 189–192.